Prakash K. Labhane[a], Gunvant H. Sonawane* and Shirish H. Sonawane

Influence of rare-earth metal on the zinc oxide nanostructures: application in the photocatalytic degradation of methylene blue and p-nitro phenol

https://doi.org/10.1515/gps-2017-0006
Received January 20, 2017; accepted July 28, 2017; previously published online September 15, 2017

Abstract: Rare-earth cerium (Ce)-doped zinc oxide (ZnO) spherical nanoparticles were synthesized by using the co-precipitation method. The doped materials were characterized by means of the X-ray diffraction, Williamson-Hall Plot, and field emission scanning electron microscopy analyses. The prepared nanoparticles exhibit a hexagonal wurtzite structure as observed from the XRD measurements. Energy dispersive X-ray spectroscopy data confirmed the purity of the prepared samples. The photocatalytic activity of the rare-earth Ce-doped ZnO spherical nanoparticles was investigated through the degradation of methylene blue (MB) and p-nitrophenol (PNP) solution under UV light radiation. Among the different amounts of dopant, 5 mole% Ce-doped ZnO nanoparticles showed the highest degradation with UV light radiation for both MB dye and PNP solution. The particle size, morphology, and separation of the photo-induced electron–hole pair are the main factors that influence photocatalytic activity. The probable mechanisms of photocatalytic degradation and mineralization of MB and PNP are also explained by liquid chromatography–mass spectrometry analysis.

Keywords: methylene blue; photocatalytic activity; p-nitrophenol; rare-earth metal; zinc oxide.

1 Introduction

The extremely high emission of organic pollutants from various industries, such as textile, printing, petroleum, pesticides, paint, and pharmaceuticals, into the aquatic medium has created serious environmental problems. Some of the organic pollutants cannot be fully degraded as they have stable chemical structures [1]. Such organic pollutants have been found to be harmful because of their non-biodegradability, high toxicity, and carcinogenic effects on humans and aquatic life [2]. Hence, their removal/degradation before discharge from the industries is a leading concern among researchers in this field. In recent years, the use of heterogeneous semiconductor photocatalysts has been attempted for the removal of organic pollutants from industrial waste due to their advantages, including high efficiency, simplicity of scale up, and low cost [3]. The different semiconductor photo catalysts have been used in the arena of the photocatalytic degradation of organic pollutants [4–6]. Among the semiconductor metal oxides, zinc oxide (ZnO) is a commonly used semiconductor because of its low cost, non-toxicity, and high surface area [7]. Remarkably, ZnO is a stable photocatalyst and is susceptible to photo-corrosion, which supports its reusability [8]. In addition, the fast recombination of the electron–hole pair in ZnO is a limiting factor in the photocatalytic degradation process. Numerous attempts have been made to improve the photocatalytic performance of ZnO [9–11]. Many researchers have attempted doping techniques of ZnO to improve its catalytic performance. Metal ions have been considered as an important dopant that can be used to regulate and improve the photocatalytic properties of ZnO [12]. In this regard, various methods have been used to produce metal ion-doped ZnO nanostructures [13–16]. Metal ions can act as electron trapping agents to hinder electron–hole recombination, thereby increasing the photocatalytic activity [17]. However, in our previous study, we noted that the transition metal-doped metal oxide can form levels deep in the band gap of semiconductor and act as recombination centers that can significantly suppress photocatalytic activity [18].

In addition to this, rare-earth metals have good thermal stability, due to their 4f electron and multi-electron arrangement. Rare-earth metals can trap photoinduced electrons, thereby reducing the recombination of the electron–hole pairs [19]. The studies of Zong et al. [20] and Korake et al. [21] explored the high photocatalytic activity of Eu-doped ZnO nanoparticles. Khatamian et al.

[a]Present address: MGSM's Arts, Science and Commerce College, Chopda, District Jalgaon (M.S.), India
***Corresponding author: Gunvant H. Sonawane,** Kisan Arts, Commerce and Science College, Parola, Dist. Jalgaon (M.S.), India, e-mail: drgunvantsonawane@gmail.com
Prakash K. Labhane: Kisan Arts, Commerce and Science College, Parola, Dist. Jalgaon (M.S.), India
Shirish H. Sonawane: Chemical Engineering Department, National Institute of Technology, Warangal-506 004 (Telangana), India

[22] successfully synthesized Ln (La, Nd or Sm)-doped ZnO nanoparticles and studied their photocatalytic activity in the degradation of p-nitrophenol (PNP). It has been found that the Ln-doped ZnO nanoparticles have a higher rate of PNP degradation compared with the undoped ZnO [23]. Amongst others, Ce-doped ZnO have attracted much attention due to the Ce^{3+}/Ce^{4+} redox couple, which influences the photo-induced charge generation and transfer, together with the elimination of the electron–hole recombination [24]. The use of rare-earth metal as a dopant has also received great attention due to its atypical properties arising from the availability of the 4f shell. To the best of our knowledge, only a few studies have reported the photocatalytic degradation of organic pollutants by the ZnO nanoparticles doped with rare-earth metal ions. The aim of this study was to analyze the physical parameters and photocatalytic activity of Ce-doped ZnO with different contents of Ce in the degradation of methylene blue (MB) and PNP, along with the degradation of the intermediate products.

2 Materials and methods

2.1 Materials

For the synthesis of the ZnO nanoparticles, analytical-grade zinc nitrate Zn $(NO_3)_2$ $6H_2O$ cerium nitrate hexahydrate [Ce $(NO_3)_2 \cdot 6H_2O$] was procured from (MDB Chemicals Pvt. Ltd., Jalgaon, MS India). Millipore deionized water was used throughout the experimentation. All the chemicals were used as they were received from the supplier without further purification. All the reagents and chemicals was from Merck, India. Origin 6.0 professional was used to draw the plots and graphs. Chem draw 8.1 was used to write chemical reactions.

2.2 Synthesis of Ce-doped ZnO nanoparticles

Undoped and Ce-doped ZnO nanostructures were prepared by following the simple co-precipitation technique using zinc nitrate [Zn $(NO_3)_2$ $6H_2O$] as the substrate precursor for the preparation of the ZnO; Ce nitrate hexahydrate [Ce $(NO_3)_2 \cdot 6H_2O$] was used as a precursor for dopant loading. In brief, the process begins with the dissolution of zinc nitrate [Zn $(NO_3)_2$ $6H_2O$] in ethanol. Suitable amounts of Ce nitrate (Ce/Zn being 3%, 5%, and 8 % molar ratios) were added to the above solution under vigorous agitation. A known amount of NaOH dissolved in deionized water was added dropwise to the above vigorously stirred solution. After 2 h of stirring, the colloids were dispersed using sonication (20 mm probe, Dakshin Ultrasound 22 KHZ 120 W) for 15 min at room temperature. The synthesized and doped ZnO material were collected by filtration, washed several times with deionized water, and then dried at 80°C for 18 h (overnight). After grinding, the samples were calcined at 550°C for about 4 h in a muffle furnace. The flowchart for the synthesis of the Ce-doped ZnO nanostructures is shown in Figure 1.

2.3 Characterization

The structural information of the undoped and Ce-doped ZnO samples were recorded in the range of 20°–80° at room temperature on Brucker D8 advance powder diffractometer (Cu Kα radiations λ = 1.5416Å). The morphology and purity of the samples were investigated with field emission scanning electron microscope (FESEM) from Hitachi. The intermediates produced by photocatalytic degradation were analyzed by liquid chromatography–mass spectrometry (LC–MS).

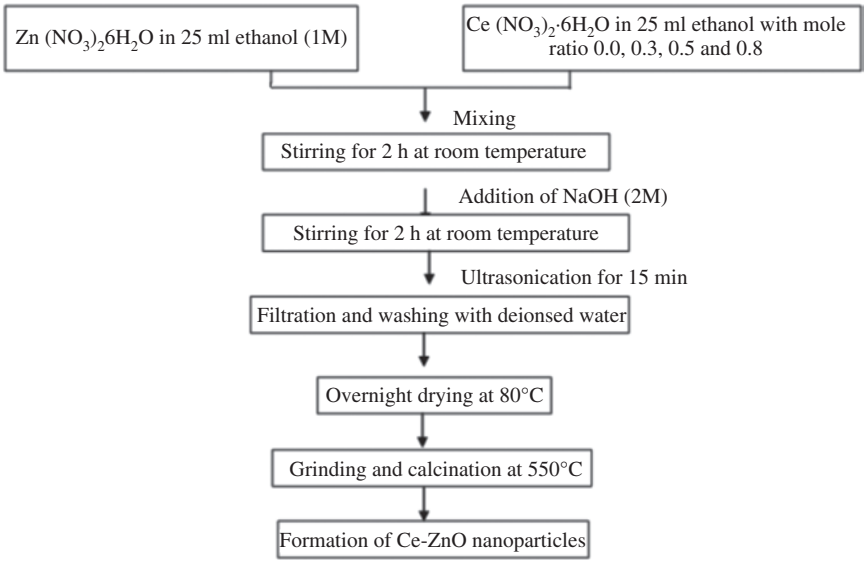

Figure 1: Schematic diagram of the Ce-doped ZnO nanoparticle synthesis.

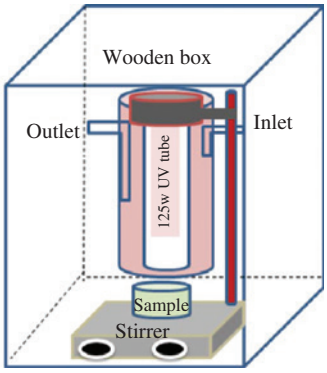

Figure 2: Schematic diagram of the photocatalytic experimental setup.

2.4 Photocatalytic experiment

Photocatalytic experiments were performed using a 125-W UV lamp as a light source placed vertically in a batch reactor. The reactor was surrounded by a cooling jacket circulated with water to control the temperature. The schematic diagram of the photocatalytic experimental setup is shown in Figure 2. The photocatalytic analysis of undoped and Ce-doped ZnO nanoparticles was carried out through the degradation of an aqueous solution of two different organic pollutants (MB and PNP) under UV light illumination. The prepared solution (25 ml, 20 ppm with 20 mg catalyst) was placed in a dark spot for 30 min to reach the equilibrium between the MB solution and the catalyst. Then, the solution was exposed to the UV radiation. Aliquots (10 ml) were collected from the above solution at regular time intervals. The collected aliquots were subjected to centrifugation and the supernatants were used to record the absorption spectra on a Shimadzu UV-1800 spectrophotometer. After recording the spectra, the collected aliquots were transferred into the previous dye solution. The degradation of the organic pollutants was monitored by UV-visible absorption spectroscopy in the wavelength range of 200–800 nm with distilled water as the reference medium. All the experiments were carried out at identical conditions and at room temperature. We determined the percentage removal of organic pollutants from the aqueous solution using the equation

$$\% \text{ removal} = \left[\frac{C_0 - C_t}{C_0}\right] \times 100, \quad (1)$$

where C_0 and C_t are the initial and final concentrations of the organic pollutants in the aqueous solution, respectively.

3 Results and discussion

Figure 3 shows the X-ray diffraction (XRD) patterns of undoped and Ce-doped ZnO with different amounts of cerium (0%, CEZ), (3%, CEZ3), (5%, CEZ5), and (8%, CEZ8). The dominant peaks at $2\theta \approx 30.78$, 34.29, 35.35, 46.74, 54.74, 62.09, 64.13, 66.21, 66.86, 72.26, and 74.78

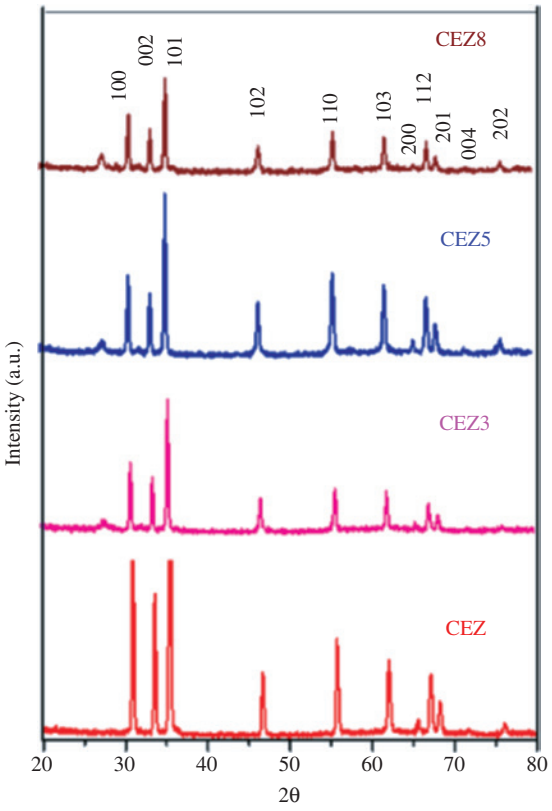

Figure 3: XRD patterns of the undoped and Ce-doped ZnO samples.

and their corresponding lattice planes (100), (002), (101), (102), (110), (103), (200), (112), (201), (004), and (202), respectively reveal that the synthesized nanoparticles exhibited good crystalline nature with a wurtzite hexagonal structure, which agreed with the JCPDS card number (01-075-1533). The c/a ratio slightly increased through the presence of Ce in the ZnO lattice and for all doped samples, the ratio is almost constant at 1.62. The results suggest that doping ZnO with Ce does not significantly alter the wurtzite ZnO nanostructures of the material. Hence, the Ce ions are incorporated into the lattice of the ZnO. Further, lower intensity peaks appeared for CEZ5 and CEZ8 at $2\theta = 28°$ and 49°, which can be attributed to the (111) and (220) planes, respectively, thereby confirming the formation of the secondary phase of CeO_2 [25]. No other impurity peaks are observed in the XRD pattern of the Ce-doped ZnO nanoparticles, which suggest that the Ce ions are uniformly substituted into the ZnO lattice. Moreover, with increasing Ce concentration, the intensity of the prominent diffraction peaks decreased and the peaks shifted marginally towards a lower angle. These results suggest that Ce doping decreased the crystalline quality and crystallite size as well as altered the lattice parameter values of the ZnO

Table 1: Physical parameters of the undoped and Ce-doped ZnO samples.

Samples	Lattice parameters		Volume cell (Å)^3	X-ray density	c/a ratio	Bond length (L)	Crystallite size D (nm)	W-H grain size (nm)	Strain (ε)
	a	c							
CEZ	3.2987	5.2738	49.6959	5.4416	1.5987	2.0062	36.10	50.96	0.000939
CEZ3	3.3038	5.3671	50.7318	5.3305	1.6245	2.0197	35.65	45.89	0.000684
CEZ5	3.3041	5.3647	50.7201	5.3317	1.6236	2.0195	34.78	45.59	0.000798
CEZ8	3.3044	5.3681	50.7609	5.3274	1.6245	2.02	33.22	37.87	0.000464

nanoparticles [26]. George et al. [27] reported that the interstitial incorporation of Ce ions in the ZnO lattice increased the lattice parameters, whereas the replacement of Zn ions with Ce ions tend to decrease the lattice parameters. The increase in the lattice parameters and volume reveals that larger ionic radii Ce^{+4} and Ce^{+3} (0.092 and 0.103 nm, respectively) have been successfully incorporated into the Zn^{+2} ion (0.74 A°) sites. Table 1 shows the structural data of the XRD patterns of undoped and Ce-doped ZnO nanoparticles.

The average crystalline size (D) is calculated by using the Debye Scherrer's formula [18],

$$D = \frac{K\lambda}{\beta cos\theta}, \tag{2}$$

where λ is the wavelength of the X-ray radiation ($\lambda = 1.5416$Å), K is the shape factor (0.9), β is the FWHM in the radians, and θ is the Bragg's angle in degree.

The average crystallite size decreased with the increase in the amount of Ce, indicating the formation of Ce–O–Zn on the surface of the doped samples, which may hinder the growth of the crystal grains [28]. The volume of unit cell is calculated from the values of the lattice constants by using the formula

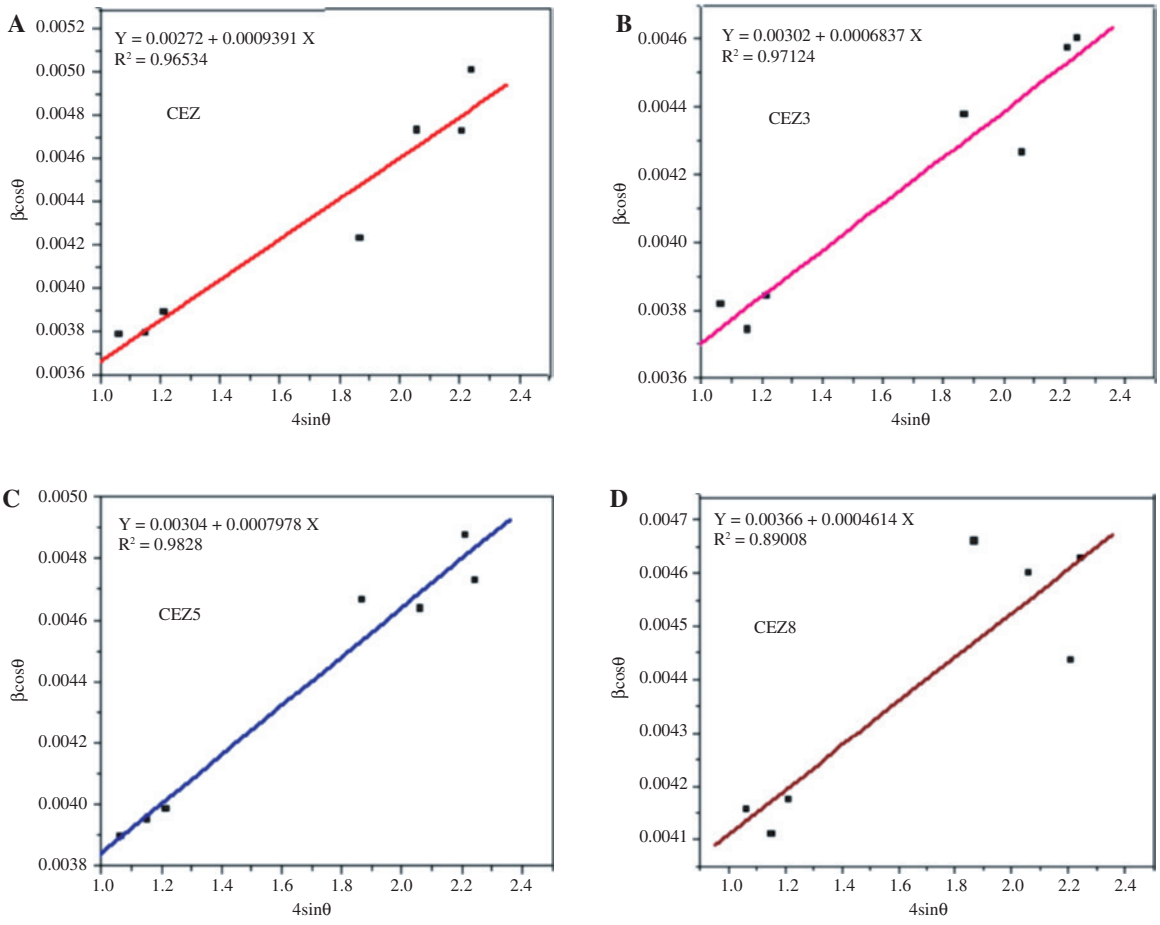

Figure 4: (A–D): The W–H plot of β_{hkl}cosθ versus 4sinθ for the undoped and Ce-doped ZnO nanostructures.

$$V = 0.866\, a^2 c. \tag{3}$$

The influence of Ce doping on the structure of the ZnO nanoparticles can be observed by calculating the Zn–O bond length "L" using the equation [29]

$$L = \sqrt{\left[\frac{a^2}{3} + \left(\frac{1}{2} - u\right)^2 c^2\right]}. \tag{4}$$

For the wurtzite structure, the u parameter is given by $u = \frac{a^2}{3c^2} + 0.25$.

The deviations observed in the volume (V) and bond length (L) values are very small, which indicate that the lattice structure of the ZnO is not altered significantly with the introduction of Ce. The calculated bond length values of all the prepared samples are tabulated in Table 1. Various peaks have been used from XRD pattern to understand the peak broadening with lattice strain. The crystalline size and strain are estimated by using the Williamson–Hall method [30], which calculates the crystallite size and strain-induced broadening using the equation

$$\beta\cos\theta = \frac{k\lambda}{D} + 4\varepsilon\sin\theta, \tag{5}$$

where β is the FWHM in radians, D is the crystalline size in nm, λ is the wavelength of the X-ray and ε is the strain. The intercept and the slope of the W–H plot of $\beta\cos\theta$ versus $4\sin\theta$ (Figure 4A–D) give the average crystallize (D) size and strain (ε), respectively. Moreover, doping of Ce results in decrease of crystallite size and lattice strain, owing to increase in lattice parameters and volume of each unit cell. From the plot, the average crystallite size and strain ε were calculated. The results are presented in Table 1.

The surface morphologies of the undoped and Ce-doped ZnO nanostructures (CEZ samples) prepared by the co-precipitation route were investigated via FESEM and are shown in Figure 5. All images clearly reveal that the average sizes of the prepared samples are in the nanometric scale. Further, the nanoparticles are uniformly distributed throughout the surface, with few agglomerations and clusters of various shapes. The size and shape of the particles also change with the increase in doping concentration, such that, with an increase in doping level of Ce

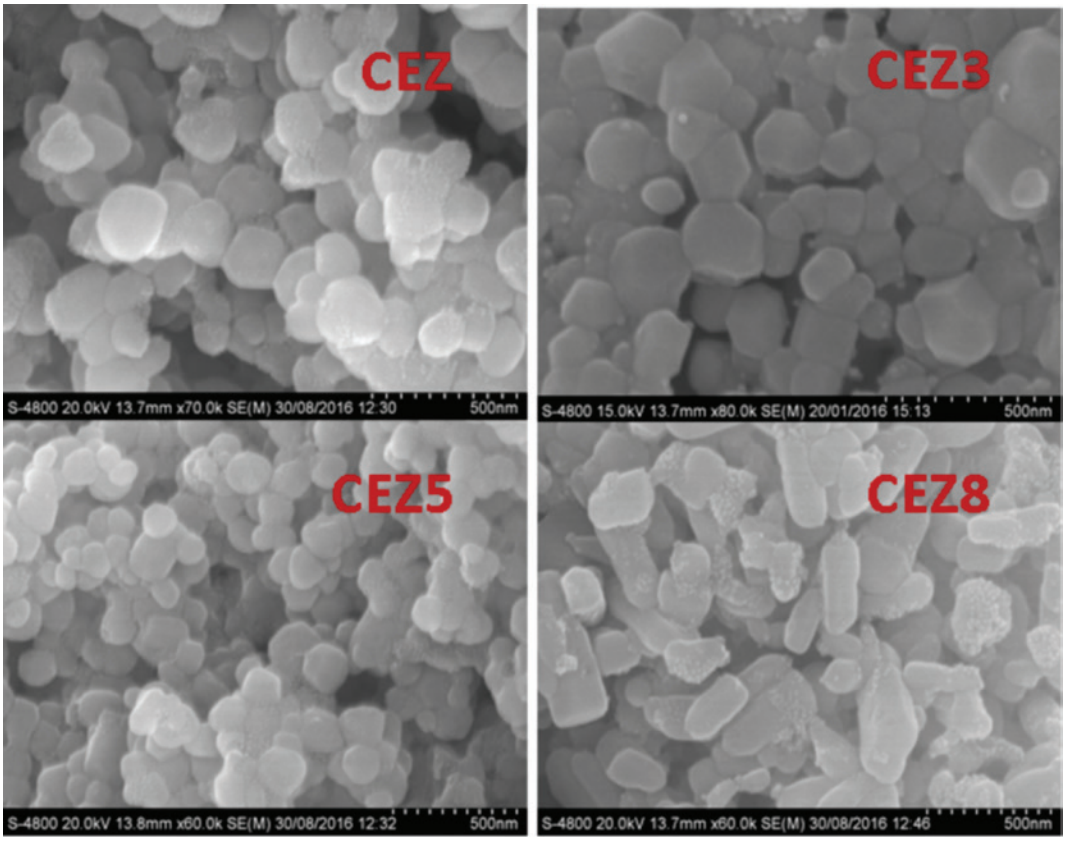

Figure 5: SEM images of the undoped and Ce-doped ZnO samples.

ions, the fairly spherical shape of nanoparticles changes to a marginally elongated shape. Li et al. [31] reported the same preferential growth in one direction in the shape of their Ce-doped ZnO. Thus, the effect of doping leads to the changes in the morphology of the nanoparticles. The elemental compositions of undoped and Ce-doped ZnO (CEZ samples) were analyzed using energy dispersive X-ray spectroscopy (EDX) analysis measurement, as shown in Figure 6. The spectra indicate the presence of Zn, Ce, and O as the major elements. EDX spectra prove the purity of the samples as there are no traces of other foreign elements.

The photocatalytic potentials of undoped and Ce-doped ZnO nanoparticles were analyzed through the degradation of MB and PNP. Figure 7A and B present the time-dependent UV-vis spectra of MB and PNP during the

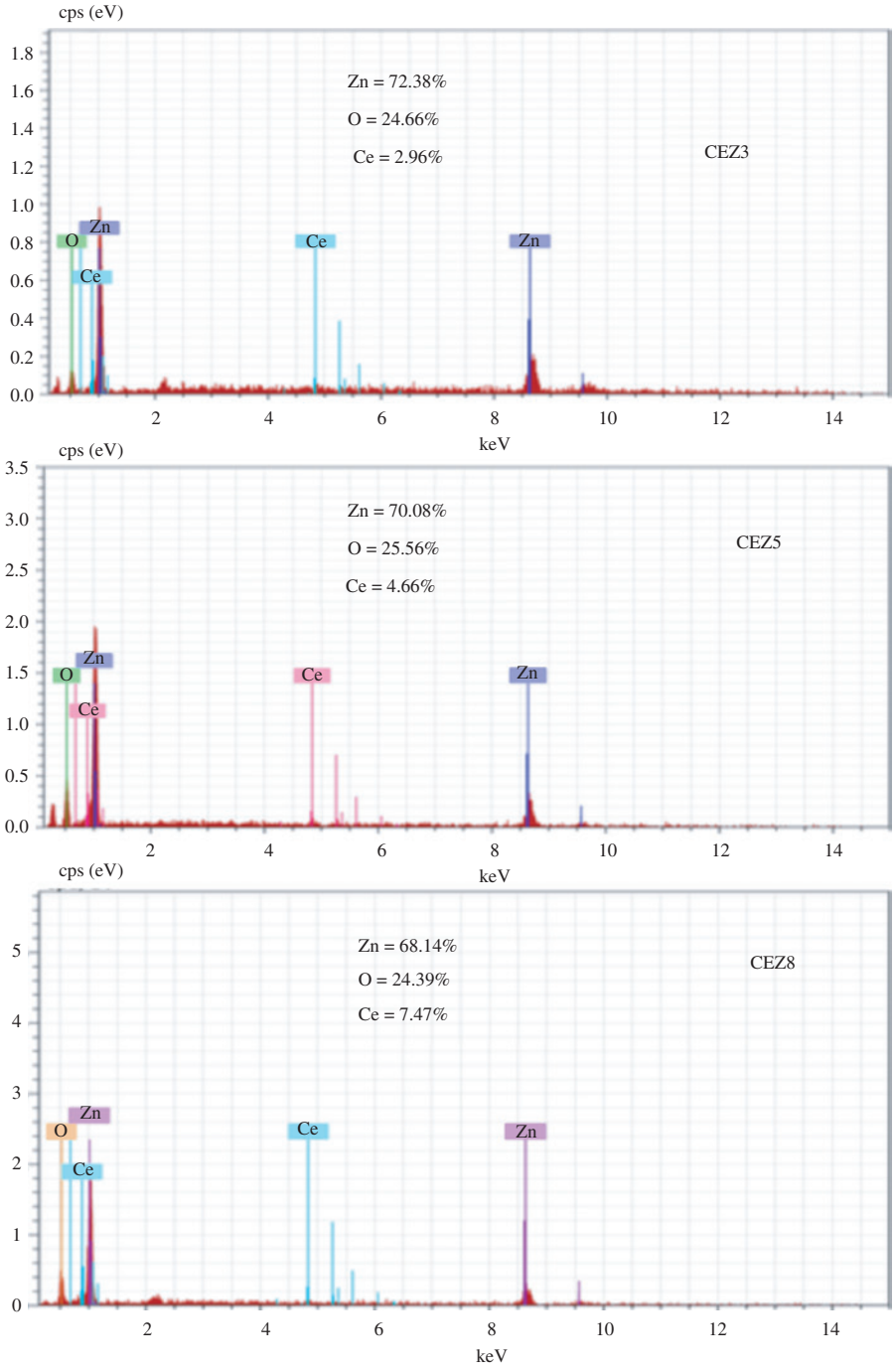

Figure 6: EDX spectra of the Ce-doped ZnO.

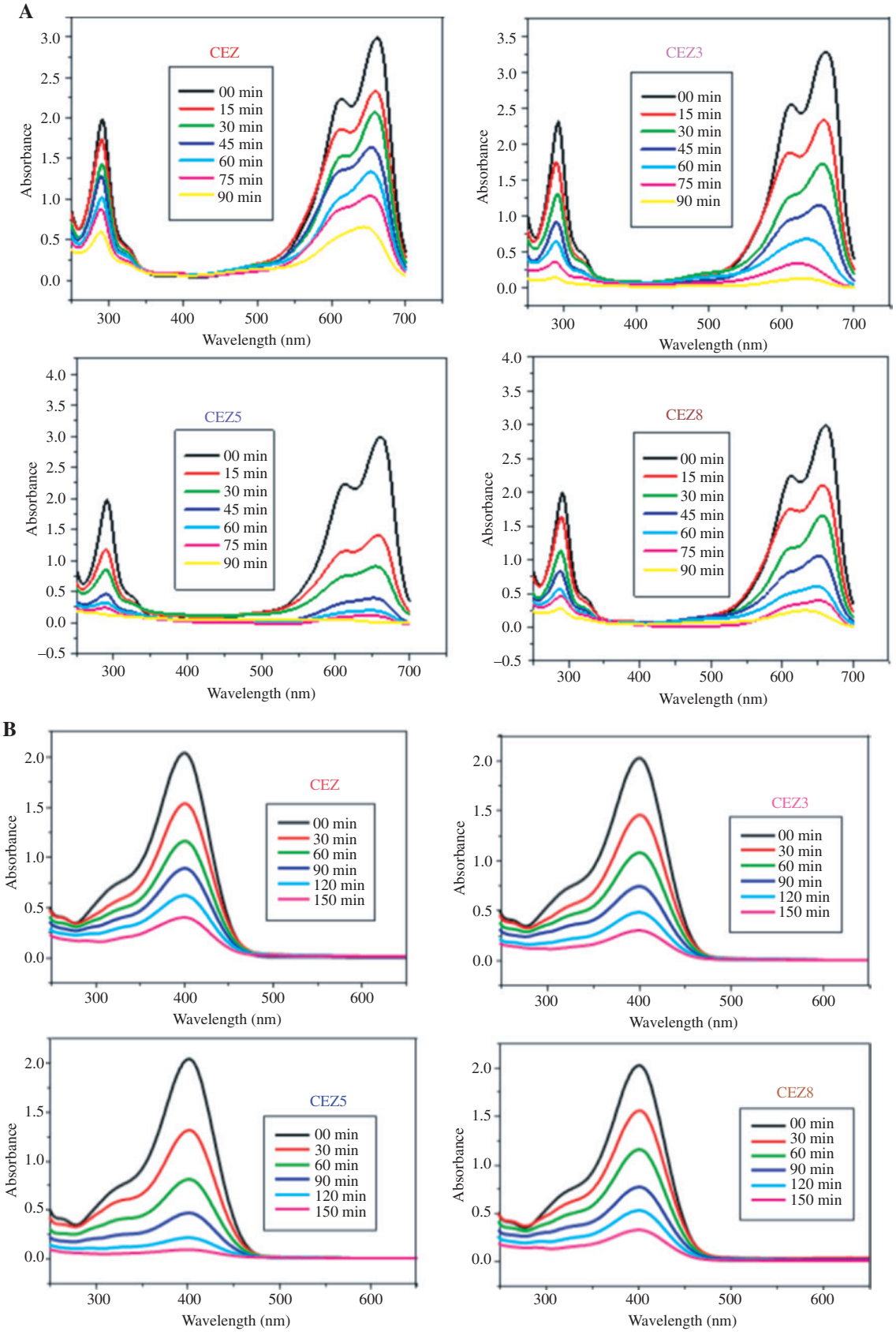

Figure 7: (A) Time-dependent UV-vis spectra of the (A) MB and (B) PNP during UV radiation with catalyst.

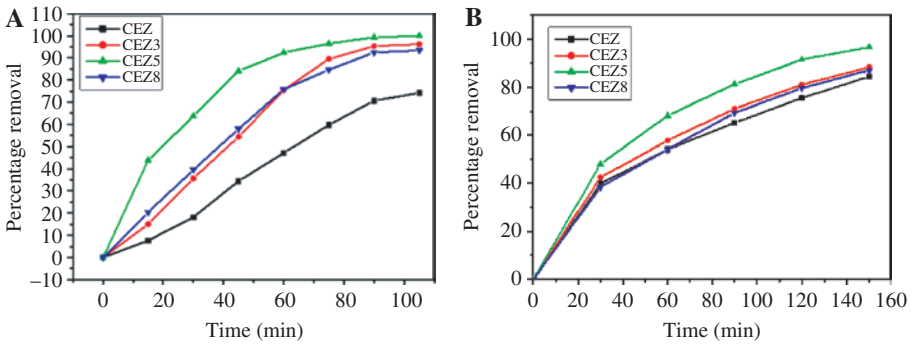

Figure 8: Percentage removal curve for the (A) MB and (B) PNP.

radiation with the catalyst. The absorption peak intensities of MB at 661 nm and of PNP at 401 nm gradually disappear with the increase in radiation times. The percentage removal curves of the MB and PNP (Figure 8A and B) indicate that the photocatalytical degradation efficiency increases with increase in Ce content. In 90 and 150 min, the concentrations were reduced by 99.9% for MB and by 97% for PNP, respectively, with the use of the 5% Ce-doped ZnO (CEZ5) photocatalyst. Further, CEZ5 has the highest photocatalytic efficiency as compared with the undoped and all other doped ZnO samples.

Many researchers reported that the photocatalytic activities of the ZnO nanomaterials strongly depend on their sizes. The nanomaterials with the smaller size exhibit better photocatalytic activity due to the higher surface area [26]. Our results also agree with this by up to 5% Ce doping level. However, the degradation efficiencies of both MB and PNP become lower with the further increase in the Ce doping concentration. On this basis, we presume that the particle size and shape would be main reason for the change of photocatalytic activity up to certain level of doping. Other factors, such as the recombination of the photogenerated electron–hole, also play very important roles in the photocatalytic activity. Moreover, rare-earth metals ions can effectively reduce the recombination of photogenerated electron–hole pairs by trapping the electrons, which in turn, facilitates the efficient separation of the photoinduced electrons and limits the charge recombination in the electron-transfer processes [32]. Further, Ce ions exist in two oxidation states: Ce^{3+} and Ce^{4+} at the catalyst surface [33]. Ce^{4+}-doped ZnO would increase surface defects, which can enhance the photocatalytic efficiency. Ce^{4+} ions can act as a scavenger by trapping the conduction band electrons, and reduce into Ce^{3+}, which can decrease electron–hole recombination. The photogenerated h+ on the catalyst surface go through charge transfer with the adsorbed water molecules to generate the active hydroxyl radical (˙OH). Further, the reduction of molecular O_2 by the photogenerated electron results in the generation of the $\dot{O}_2^-$ radicals. A scavenger study revealed that hydroxyl radicals and super oxide radicals are the active species responsible for the photodegradation of MB and PNP [34]. The expected plausible mechanisms of MB and PNP degradation are presented in Figure 9. As can be seen, the photocatalyst CEZ5 exhibited higher catalytic efficiency for both the MB and PNP. However, when the amount of Ce^{4+} ions is higher than the optimum amount (5%), the high concentration of Ce ions act as the recombination centers of electrons and hole, hence decreasing the photocatalytic activity.

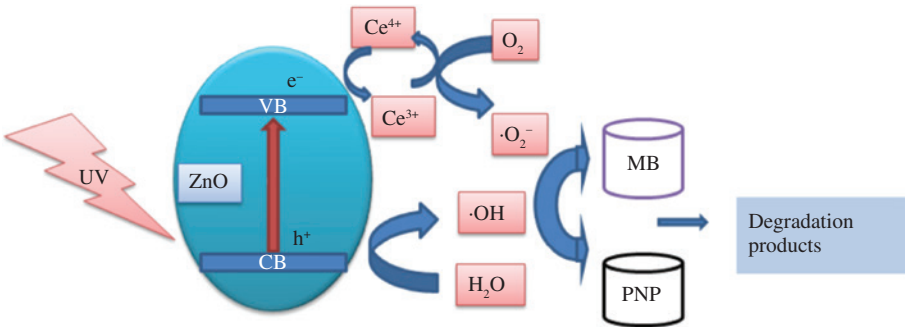

Figure 9: Plausible mechanism of the degradation of the MB and PNP.

Table 2: Average decoloration rates for the MB and PNP.

Samples	Average decolortion rate for MB (μg/h)	Average decolortion rate for NP (μg/h)
CEZ	142.9	165.76
CEZ3	230.64	177.32
CEZ5	361.57	201.93
CEZ8	246.31	167.84

The average decolorization rates (μg/h) under the abovementioned conditions (25 ml, 20 ppm with 20 mg catalyst) are calculated by using the formula [35]

$$\text{Average decolorization rate (μg/h)} = \frac{C \times D \times 1000}{100 \times t}, \quad (6)$$

where C is the initial concentration of dye (mg/l) and D is the dye decoloration (%) after time t (h). The average decoloration rate obtained during the photocatalytic degradation of MB and PNP are tabulated in Table 2. As can be seen, CEZ5 has the highest average decoloration rate for the MB and PNP amongst all the prepared samples.

The reaction rate constants (k) for the photocatalytic degradation of MB and PNP using Ce doped ZnO nanostructures are calculated by using the equation

$$\ln\left(\frac{C_0}{C_t}\right) = kt, \quad (7)$$

where C_0 is the initial concentration, C_t is the concentration at time t, and k is the first-order rate constant. CEZ5 exhibited excellent photocatalytic performance with higher rate constants for the MB and PNP degradation, which are presented in Figure 10A, B and Table 3). The correlation coefficient values (R^2) are greater than 0.9, which indicates that the photocatalytic degradation of the MB and PNP follows the first-order kinetics.

Table 3: Rate constants (k) for the photocatalytic degradation of the MB and PNP.

Samples	Rate constant k for MB (min^{-1})	Correlation coefficient values (R^2)
CEZ	0.01454	0.97271
CEZ3	0.03183	0.98786
CEZ5	0.04591	0.99678
CEZ8	0.0269	0.99609
	PNP (min^{-1})	
CEZ	0.01172	0.995
CEZ3	0.01381	0.99742
CEZ5	0.02013	0.99913
CEZ8	0.01333	0.99836

Degradation of the MB and PNP can be explained on the basis of AOPs promoted by heterogeneous photocatalysis. This process involves the generation of e^- and h^+, which then generate the $^{\cdot}O_2^-$ and $^{\cdot}OH$ radicals, respectively. These radicals are highly reactive and act as degrading agents. In order to understand the degradation pathway and intermediates that form during the photocatalytic degradation, LC–MS analysis was carried out. The mechanistic pathway of the photodegradation of MB dye to form intermediates using the CEZ5 nanoparticles is shown in Figure 11. The initial step of the MB degradation would be to attack the $^{\cdot}OH$ radicals that convert the C–S+=C and C=N–C bonds to the C–SH $(=O)_2$–C and C–NH–C, respectively. The intermediates at m/z 301, 291, and 319 shown in Figure 11 are in accordance with the results reported by Hu et al. [36].

The PNP is very stable in the absence of catalyst under UV light radiation, but undergoes degradation in the presence of the CEZ5 catalyst under UV light, resulting in the formation of some intermediate products. The aromatic intermediates identified by the LC–MS analysis are benzoquinone (m/z 107), hydroquinone (m/z 109,)

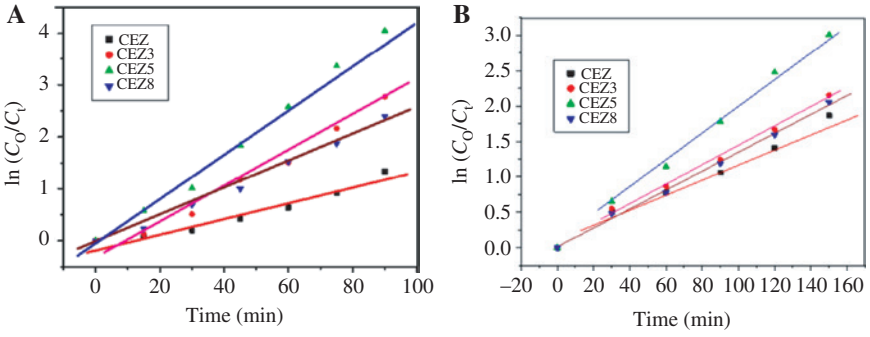

Figure 10: Plot of $\ln(C_0/C_t)$ versus time for the degradation of the (A) MB and (B) PNP.

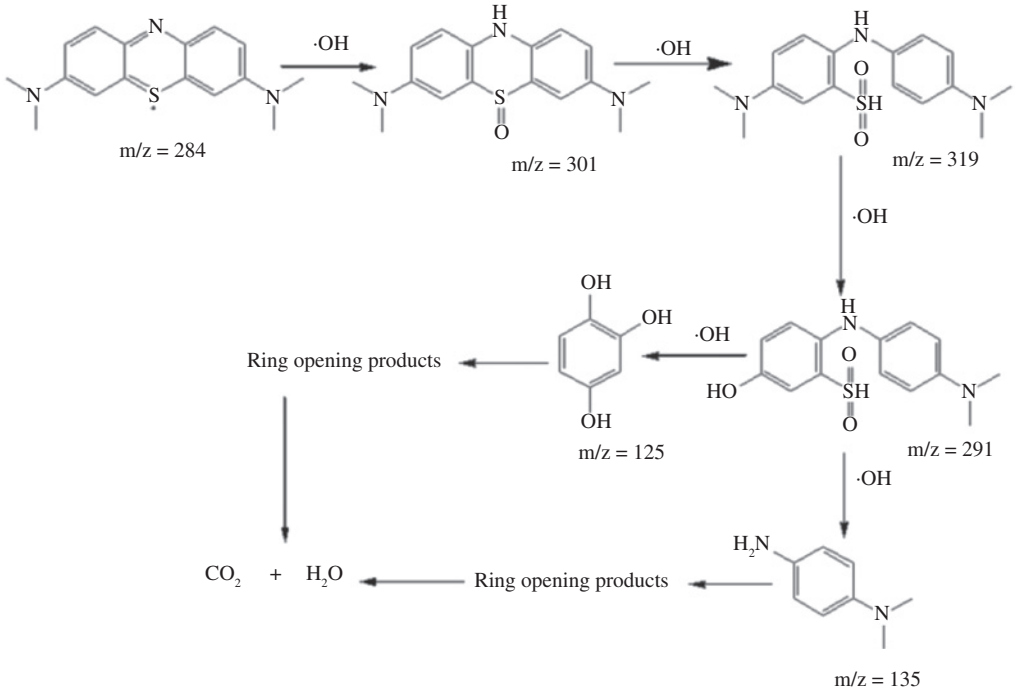

Figure 11: Probable organic intermediates of the MB on UV light radiation with the catalyst.

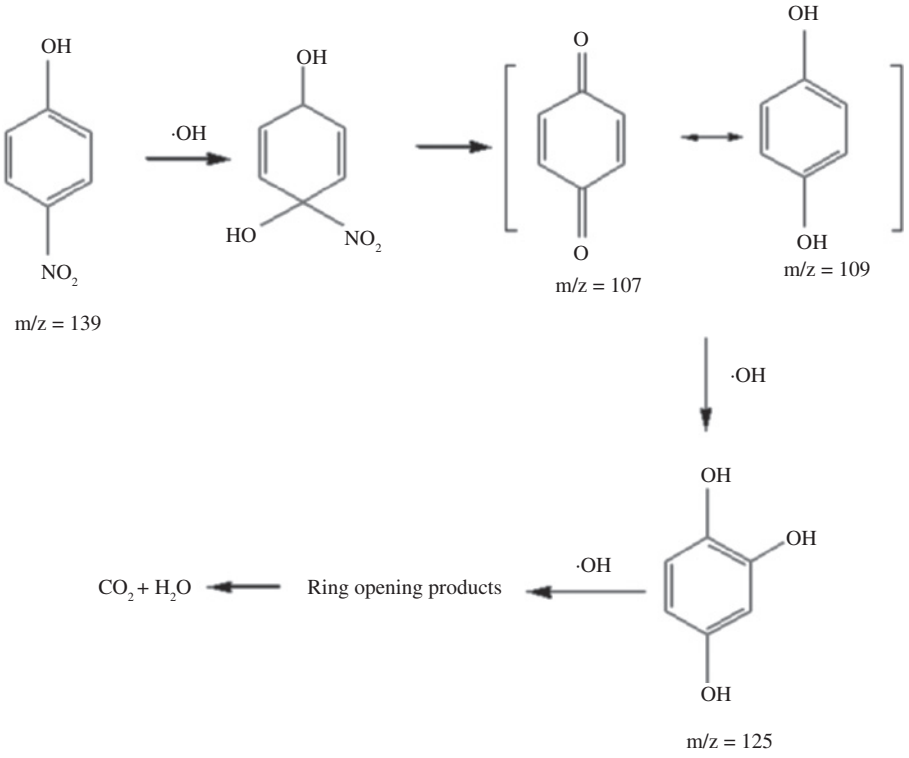

Figure 12: Probable organic intermediates of the PNP on UV light radiation with the catalyst.

and 1,2,4-trihydroxybenzene (m/z 125). The initiation of the photocatalyic degradation takes place because of the attack of the ·OH radical at the ipso position of the PNP to release the nitro group, and the aromatic ring would transform into benzoquinone and hydroquinone. Further, the phenolic group of the hydroquinone increases the

electron density at the ortho and para position and may convert the aromatic ring into 1,2,4-trihydroxybenzene. The plausible intermediate formation pathway during the catalytic oxidation of the PNP by the CEZ5 photocatalyst is shown in Figure 12.

4 Conclusions

In this study, the undoped and Ce-doped ZnO spherical nanoparticles have been successfully synthesized by using the modified co-precipitation method. XRD data revealed that the synthesized nanoparticles exhibited good crystalline nature with a wurtzite hexagonal structure. The c/a ratio slightly increased by introducing Ce into the ZnO lattice, and for all doped samples, the ratio is almost constant at 1.62. Ce doping decreased the crystallinity and crystallite size and alters the lattice parameters values of the ZnO nanoparticles. FESEM analysis confirmed the uniform distribution of the ZnO nanoparticles throughout the surface with few agglomerations and clusters of various shapes. The size and shape of particles change with the increase in doping concentration of Ce. Photocatalytic efficiency increased gradually with an increase of the Ce content up to a certain doping level for both the MB and PNP. Ce^{4+} ions also act as a scavenger to trap the conduction band electrons, which is responsible for reducing the electron–hole recombination, thereby increasing the photocatalytic efficiency. The probable intermediates of the MB and PNP during photodegradation have been described on the basis of the LC–MS analysis.

Nomenclature

C_o	initial concentration
C_t	final concentration
K	shape factor (0.9)
Λ	wavelength of X-ray radiation
β	full width half maxima (FWHM)
ε	strain

Acknowledgments: The authors wish to thank North Maharashtra University, Jalgaon, India, for providing financial support (NMU/11A/VCRMS/Budget-2015-16/Science-9/65/2016).

References

[1] Yayapao O, Titipun T, Anukorn P, Somchai T. *Mater. Sci. Semicond. Process.* 2015, 39, 786–792.
[2] Goyal A, Bansal S, Singhal S. *Int. J. Hydrogen Energy* 2014, 39, 4895–4908.
[3] Tokode O, Radhakrishna P, Lawton LA, Robertson PK. *J. Photochem. Photobiol. A Chem.* 2016, 319, 96 –106.
[4] Bethi B, Shirish H, Sonawane BA, Gumfekar SP. *Chem. Eng. Process. Process Intensification* 2016, 109, 178–189.
[5] Sudha D, Sivakumar P. *Chem. Eng. Process. Process Intensification* 2015, 97, 112–133.
[6] Sreethawong T, Supachai N, Yoshikawa S. *Chem. Eng. J.* 2013, 228, 256–262.
[7] Hemalatha P, Karthick SN, Hemalatha K, Yi MS, Kim H-J, Alagar M. *J. Mater. Sci. Mater. Electron.* 2016, 27, 2367–2378.
[8] Chang X, Li Z, Zhai X, Sun S, Gu D, Dong L, Yin YS, and Zhu Yanqiu. *Mater. Des.* 2016, 98, 324–332.
[9] Torres-Hernández JR, Ramírez-Morales E, Rojas-Blanco L, Pantoja-Enriquez J, Oskam G, Paraguay-Delgado F, Escobar-Morales B, Acosta-Alejandro M, Díaz-Flores LL, Pérez-Hernández G. *Mater. Sci. Semicond. Process.* 2015, 37, 87–92.
[10] Zhai YJ, Li JH, Fang X, Chen XY, Fang F, Chu XY, Wei ZP, Wang XH. *Mater. Sci. Semicond. Process.* 2014, 26, 225–230.
[11] Divya NK, Pradyumnan PP. *Mater. Sci. Semicond. Process.* 2016, 41, 428–435.
[12] Yousefi R, Jamali-Sheini F, Cheraghizade M, Khosravi-Gandomani S, Sáaedi A, Huang NM, Basirun WF, Azarang M. *Mater. Sci. Semicond. Process.* 2015, 32, 152–159.
[13] Mardani HR, Forouzani M, Ziari M, Biparva P. *Spectrochim. Acta A Mol. Biomol. Spectrosc.* 2015, 141, 27-33.
[14] Cho S, Jang J-W, Lee JS, Lee K-H. *CrystEngComm* 2010, 12, 3929–3935.
[15] Raja K, Ramesh PS, Geetha D. *Spectrochim. Acta A Mol. Biomol. Spectrosc.* 2014, 120, 19–24.
[16] Rezaei M, Habibi-Yangjeh. *Mater. Lett.* 2013, 110, 53–56.
[17] Wang Y, Zhao X, Duan L, Wang F, Niu H, Guo W, Ali A. *Mater. Sci. Semicond. Process.* 2015, 29, 372–379.
[18] Labhane PK, Huse VR, Patle LB, Chaudhari AL, Sonawane GH. *J. Mater. Sci. Chem. Eng.* 2015, 3, 39.
[19] Kuzhalosai V, Subash B, Shanthi M. *Mater. Sci. Semicond. Process.* 2014, 27, 924–933.
[20] Zong Y, Li Z, Wang X, Ma J, Men Y. *Ceram. Int.* 2014, 40, 10375–10382.
[21] Korake PV, Kadam AN, Garadkar KM. *J. Rare Earths* 2014, 32, 306–313.
[22] Khatamian M, Khandar AA, Divband B, Haghighi M, Ebrahimi-asl S. *J. Mol. Catal. A Chem.* 2012, 365, 120–127.
[23] Chang C-J, Lin C-Y, Hsu M-H. *J. Taiwan Inst. Chem. Eng.* 2014, 45, 1954–1963.
[24] Kannadasan N, Shanmugam N, Cholan S, Sathishkumar K, Viruthagiri G, Poonguzhali R. *Mater. Charact.* 2014, 97, 37–46.
[25] Ojha GP, Pant B, Park S-J, Park M, Kim H-Y. *J. Colloid Interface Sci.* 2017, 494, 38–344.
[26] Li X, Wang J, Yang J, Lang J, Cao J, Liu F, Fan H, Gao M, Jiang Y. *Mater. Chem. Phys.* 2013, 141, 929–935.
[27] George A, Sharma SK, Chawla S, Malik MM, Qureshi MS. *J. Alloys Compd.* 2011, 509, 5942–5946.
[28] Bechambi O, Touati A, Sayadi, Najjar W. *Mater. Sci. Semicond. Process.* 2015, 39, 807–816.
[29] Khan M, Xu J, Chen N, Cao W. *J. Alloys Compd.* 2012, 513, 539–545.
[30] Stokes AR, Wilson AJC. *Proc. Phys. Soc.* 1944, 56, 174–174.

[31] Li G-R, Lu X-H, Zhao W-X, Su C-Y, Tong Y-X. *Cryst. Growth Des*. 2008, 8, 1276–1281.
[32] Zhang N, Chen D, Niu F, Wang S, Qin L, Huang Y. *Sci. Rep.* 2016, 6, 1–11.
[33] Anandan S, Miyauchi M. *Phys. Chem. Chem. Phys*. 2011, 13, 14937–14945.
[34] Labhane PK, Patle LB, Huse VR, Sonawane GH, Sonawane SH. *Chem. Phys. Lett.* 2016, 661, 13–19.
[35] Rauf MA, Meetani, MA Khaleel A, Ahmed A. *Chem. Eng. J.* 2010, 157, 373–378.
[36] Hu YL, Zhou LQ, Liu HF, Guo XP. *Key Eng. Mater*. 2014, 609, 141–146.